Correspondence to:
M. Derakhti,
derakhti@uw.edu

Temporal and Topographic Source Effects on Tsunami Generation

Morteza Derakhti[1] , **Robert A. Dalrymple[2]**, **Emile A. Okal[3]**, and **Costas E. Synolakis[4]**

[1]Applied Physics Laboratory, University of Washington, Seattle, WA, USA, [2]Department of Civil and Environmental Engineering, Northwestern University, Evanston, IL, USA, [3]Department of Earth and Planetary Sciences, Northwestern University, Evanston, IL, USA, [4]Department of Civil and Environmental Engineering, University of Southern California, Los Angeles, CA, USA

Abstract We present a systematic study of the influence on tsunami waves generated by the uplift of a rectangular plug, of the rise time of the deformation, and of its topographic details (e.g., the presence of a sill). We are motivated by the fact that most simulation codes use an instantaneous deformation of a flat ocean floor as an initial condition of the problem, although Hammack (1973, http://resolver.caltech.edu/CaltechAUTHORS:HAMjfm73) performed pioneering laboratory studies as well as analytical computations featuring variable rise times. Here, we consider three 2-D source shapes, including a flat seafloor, a simple elevated piston, and additional trapezoidal sill on top of it, all with variable rise times, and simulate the resulting waves using the fully nonlinear smooth particle hydrodynamic model graphics processing unit smooth particle hydrodynamic. We validate our results against Hammack's (1973) laboratory measurements and analytical results. We find that a relatively large sill, with height and width of more than half of the local depth and width of the source, has a profound effect on the spatiotemporal structure of the generated free surface wavefield. Specifically, we show that the maximum water surface elevation over the source region is not always the same as the bottom displacement, as assumed in most tsunami propagation models. Next, we obtain simple scaling relationships to predict the maximum height of the generated tsunami over and outside the source, based on the geometry of the sill and the nondimensional bed rise time. Last, we show that inertial effects may lead to an initial free surface displacement over the generation region greater than the maximum vertical displacement of the displaced seabed.

1. Introduction

The purpose of this paper is to provide a detailed discussion of the near-field evolution of the tsunami produced by an idealized bottom displacement that distinguishes impulsive bottom motions from slower ones. In very general terms, the tsunami phenomenon may be divided into three stages (Gisler, 2008; Voit, 1987): formation of the tsunami and its propagation near the source (Hammack, 1973; Jamin et al., 2015; Kajiura, 1972; Kervella et al., 2007; Nosov, 1999, 2014; Nosov & Kolesov, 2007; Stefanakis et al., 2015; Ward, 1980), hereafter referred to as near-field evolution; free propagation of the tsunami in the open ocean (Glimsdal et al., 2006; Titov et al., 2005; Okal, 1988; Okal & Synolakis, 2008, 2016); and finally propagation and run-up in coastal regions while interacting with topography features and infrastructures (Muhari et al., 2011; Okal & Synolakis, 2004; Park et al., 2013; Shimozono et al., 2014; Son et al., 2011; Wei et al., 2015, 2016).

One major cause of tsunamis is the rapid vertical displacement of an area of the seabed due to an underwater earthquake. This bottom displacement ξ forces the water above the source upward (or downward), resulting in a corresponding displacement η of the free surface. This initial free surface displacement is often taken to be the same as the bottom displacement ($\eta = \xi$) when prescribing the initial condition for tsunami simulations that propagate the tsunami away from the source area to land (Ichinose et al., 2003; Synolakis, 2003). That approach is based on a classic result of one-dimensional wave theory, where instantaneous forcing is equivalent to assignment of an initial condition to the free surface (Saito & Furumura, 2009; Synolakis, 2003). However, the water surface displacement above the source area only matches the bottom displacement under certain conditions, and an important aspect of the present study is that it quantifies the limitation (in terms of rise times) of this ubiquitous assumption in tsunami simulations, namely, that the deformation of the ocean floor can be directly transposed to the top of the water column.
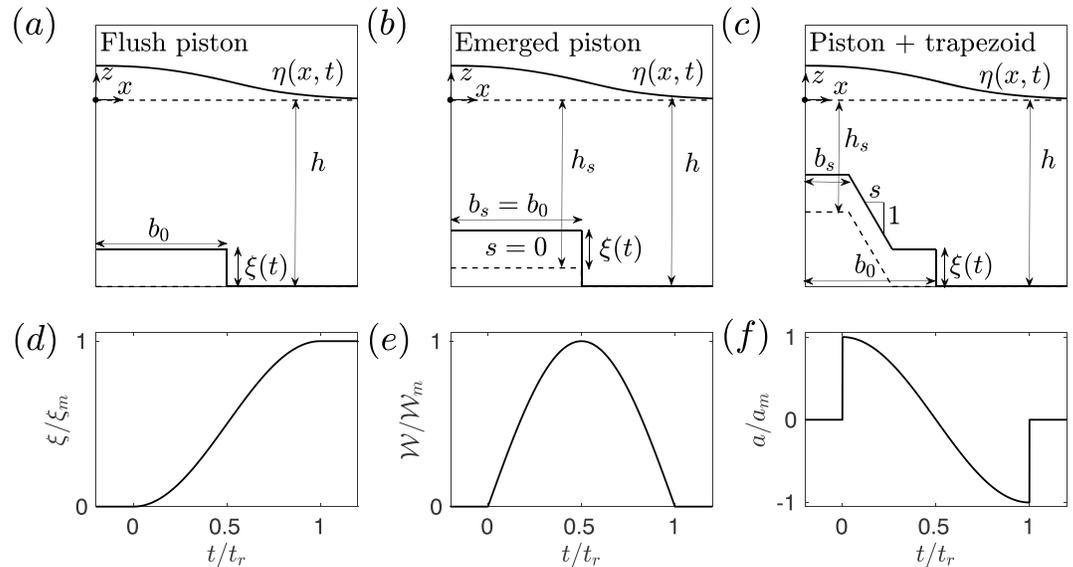
Figure 1. Schematic of the side view of half of the computational domain ($x \geq 0$) for a (a) flush piston, (b) emerged piston, and (c) piston with a trapezoid on its top, as well as the temporal variation of the normalized vertical (d) displacement, (e) velocity, and (f) acceleration of the source for the deformation scenario given by equation (5). Here, ξ_m, $\mathcal{W}_m$, and a_m are the maximum vertical displacement, velocity, and acceleration of the source respectively, and t_r is the bed rise time. In (a)–(c), the dashed and solid lines show the water boundaries before and after the initiation of the bed movement, respectively.

We are motivated by the need to model real-case scenarios of tsunami generation in the geological environment where this "direct transposition" may not apply. For example, a clear violation would be the case of the interseismic interval at a subduction zone, which lasts typically one or more centuries. We know that no tsunamis are generated in between two megathrust earthquakes, as the plate interface deforms slowly through buckling at rates of at most a few centimeters per year. This is explained physically by noting that such a deformation occurs so slowly that the mass of water displaced by each of its infinitesimal steps has time to readjust itself to equilibrium before the next step; in other words, the interseismic deformation is achieved reversibly from a thermodynamic point of view, and no wasted energy is available to generate a tsunami. While common sense dictates that interseismic creeping motions at such slow rates should not generate tsunamis, the question remains open of the precise quantification of the rates of deformation at which tsunami genesis disappears, notably in view of the recent identification of different types of slow tectonic deformation.

In very simple terms and, as will be discussed more in detail in section 5, in the case of traditional earthquakes obeying scaling laws, the rise time t_r (i.e., the time it takes for individual elements of the dislocation to physically move to their displaced location) grows as the cubic root of the seismic moment M_0 of the earthquake, from ~1 s for a small earthquake of moment 10^{25} dyn.cm ($M_w = 5.9$) to a maximum of about 75 s for the largest earthquake ever recorded ($M_0 = 2 \times 10^{30}$ dyn.cm; Chile, 1960; e.g., Geller, 1976).

By contrast, and as summarized, for example, by Beroza and Ide (2011), a number of phenomena involving much longer rise times have been documented in the past two decades, from both long-period seismic records and modern geodetic surveys using continuous GPS. They include "very slow earthquakes" featuring rise times of up to 200 s for minimal seismic moments ($M_0 = 10^{22}$ dyn.cm, or $M_w = 4$) and "slow slip events," which may involve moments of up to 10^{27} dyn.cm, but with source times as long as tens to hundreds of days. Even though some of these sources occur at significant depth (50–80 km) along the subduction interface (e.g., Schwartz & Rokosky, 2007), they establish the existence among tectonic processes of a wide diversity in source duration, thus warranting the systematic study of the influence of rise time on tsunami genesis, which is the subject of this paper.

As shown on Figure 1, the problem can be investigated by considering an ocean of depth h, and a source of half-width b_0, displaced upward a total amount ξ_m over a rise time t_r. In this context, we can define three dimensionless parameters, namely, a geometric aspect ratio of the source b_0/h; the ratio ξ_m/h, a function of

the total amplitude of the phenomenon (which as such will control any nonlinearity of the solution); and the dimensionless ratio:

$$\tau = \frac{t_r}{t_c}, \tag{1}$$

which Hammack (1973) has called the time-size parameter. This is the ratio of the rise time to the time $t_c = b_0/\sqrt{gh}$ it takes a long wave with speed $\sqrt{gh}$ to propagate a distance equal to half the source width and hence disseminate the initial disturbance of the surface out of the source area, g being the acceleration of gravity. Once a solution to the hydrodynamic equations is obtained, the amplitude of the wave at the surface can be expressed through the additional dimensionless ratio η_m/ξ_m, which is thus a function of the other three; it can be used to quantify the validity of the approximation of the initial conditions in classical hydrodynamic simulations.

There have been numerous analytical solutions to the bottom displacement tsunami problem using potential flow and linear wave assumptions (e.g., Hammack, 1973; Ichiye, 1958; Kajiura, 1963). These solutions have been obtained in a variety of ways (e.g., Green's functions, Kajiura, 1963; Fourier-Laplace transforms, Hammack, 1973; and Fourier-Bessel transforms, Ward, 2001).

In a landmark study using linear analysis and laboratory experiments, Hammack (1973) showed that the ratio between the surface and bottom displacements depends critically on the *time-size ratio*, τ. He also showed that the longer the uplift time, the smaller the surface-to-bottom ratio, η_m/ξ_m, and that the width of the source was also important—the smaller the source area, the smaller the free surface displacement. The laboratory study of Hammack (1973) elucidated the main dynamics of near-field surface wave generation due to an idealized bed motion identifying three regimes, which he named impulsive ($\tau \ll 1$, in which a large displacement is generated before water can flow away from the source area), transitional ($\tau \approx 1$), and creeping ($\tau \gg 1$, in which little or no wave is generated in the far field, as the source is too slow to accumulate a sufficient mass of water in the source area before it flows away). The maximum elevation of the leading wave radiating into the far field ($x \gg b_0$) was found to be a decreasing function of τ, bounded in all cases by one half of the maximum vertical displacement of the bed at the source. Hammack (1973) further showed that linear theory is appropriate as long as $\xi_m/h \ll 1$, and $\tau(\xi_m/h) \ll 1$. Here we will elaborate on his results and in particular use his laboratory data as a set of observables against which we test our computations.

Using a numerical technique to solve the tsunami problem and allowing a finite time for the bottom uplift, Saito and Furumura (2009) showed that the free surface displacement is smaller than the bottom displacement when the water depth over the source is large, or when the time of uplift is long. They also showed that the initial free surface displacement is smaller than the bottom displacement when the water is deep or the spatial extent of the source is small. All these conditions leading to a decrease in η_m/ξ_m simply contribute to an increase in τ, by either lengthening the rise time or shortening the source area b_0 over which, or accelerating the speed $\sqrt{gh}$ at which, the water is expelled. Finally, Saito and Furumura (2009) showed that the initial water motion over the source area is vertical, while the bottom is moving upward and then as the bottom motion stops the velocities become horizontal over the water column as the initial free surface displacement transforms into propagating waves.

Ichiye (1958) assumed the earthquake could be represented by an imposed constant vertical velocity at the bottom during the time $0 < t < t_r$, the bottom velocity becoming 0 for $t \geq t_r$. He showed results for a single case for $b_0/h = 10$ and $\tau = 0.04$. The maximum displacement of the free surface occurred at $t = t_r$. Since Ichiye's approach has no actual bottom displacement, his results would be limited to $\xi_m/h \ll 1$ as expected. Kajiura (1963) assumed instantaneous faulting of the bottom, neglecting the effect of dimensionless rise time, τ. He showed that the initial free surface displacement for an instantaneous bottom uplift is always less than the magnitude of the bottom displacement except when the source is large with respect to the depth, $b_0/h \gg 3$.

However, in most of the previous near-field analytical, numerical and experimental studies, including Hammack's (1973), the moving bed is initially at the same elevation as the adjacent fixed bed. In the framework of linear shallow-water wave theory, Kajiura (1972) examined tsunamis and edge waves generated by an abrupt seabed movement on or near a step-like shelf and found that the wave energy radiated into the deep water decreased in the presence of the shelf. Stefanakis et al. (2015) further investigated analytically the effect of a cylindrical sill on the tsunami in the far field and found that, as the sill height is increased, partial wave trapping reduces the leading wave height in the far field while amplifying it above the sill. These

results are in general agreement with the concept of Green's law (Green, 1837; Synolakis, 1991); they help explain, for example, the deficient far-field amplitude of the 2005 Nias tsunami, as modeled by Synolakis and Arcas (quoted by Kerr, 2005).

Because seafloors are never flat and can feature seamounts and canyons whose effects on wave generation are little understood, a number of relevant questions remain as to how the width of a sill relative to that of the moving element of the seabed, as well as its side slopes, can affect the generation of a tsunami. In this context, a main goal of this paper is examination of the effect of the spatial structure of large seabed topographic features on the near-field dynamics of tsunamis generated by both relatively fast and slow sources. In particular, we will examine how the relative height, width, and slope of an idealized submerged sill affect the generated wavefield.

Our analysis is carried out using the fully nonlinear and dispersive Smooth Particle Hydrodynamic (SPH) model GPUSPH (Hérault et al., 2010), which includes fluid inertia and wave amplitude effects. Further, our results are directly applicable to studies of the effect of the tsunami on shorelines in the vicinity of the source, for which propagation effects are small. The mathematical formulation together with the model setup are briefly explained in section 2. Then, in section 3, we compare our results with the laboratory data of Hammack (1973). Further, we examine the inertia effects on the initial free surface displacement over the generation region. In section 4, we discuss our findings for a wide range of seafloor features and temporal variations. The last two sections discuss them in a geophysical setting, in terms of realistic earthquake generation parameters, and summarize our findings.

2. Numerical Simulations

In this section, we present the equations for continuity of mass and momentum solved by the SPH model GPUSPH, as well as the model setup including details of the bed deformation. The interpolation scheme for the Eulerian velocity and pressure fields is then explained.

2.1. Mathematical Formulations

GPUSPH (http://www.gpusph.org) is an open-source implementation of the weakly compressible SPH method on GPUs. In the SPH method, continuity and momentum equations are discretized on a number of nodes (particles) using an interpolation kernel (Monaghan, 1992, 2005). Details of the current numerical method may be found in Dalrymple and Rogers (2006).

The computations are performed in a Lagrangian scheme at moving computational nodes and makes use of a filtering process defined as $\tilde{f}(\mathbf{x}) = \int_V W(\mathbf{x} - \mathbf{x}', h_{sl}) f(\mathbf{x}') dV'$, where $W(\mathbf{x} - \mathbf{x}', h_{sl})$ is a spatial filter also called smoothing kernel in SPH, $h_{sl} = 1.3\Delta$ is the smoothing length, and Δ is the initial particle spacing; for convenience, we will drop the tilde in the following. The numerical results are later interpolated back into an Eulerian frame describing the flow at points fixed in space for analysis and plotting.

With an eddy viscosity assumption, the filtered equations for continuity of mass and momentum in a compressible fluid are given by

$$D(\rho) = -\rho \, u_{j,j} \tag{2}$$

$$D(u_i) = \frac{1}{\rho} \Pi_{ij,j} - g \delta_{3i}, \tag{3}$$

where $D(.)$ is the time derivative following the fluid particle, $(.)_{,j} = \partial(.)/\partial x_j$, ρ is the filtered density, u_i is the filtered velocity in the i direction, δ_{ij} is the Kronecker delta function, and $\Pi_{ij} = -p\delta_{ij} + \sigma_{ij} + \tau_{ij}^{sps}$ is the total stress tensor, with $\sigma_{ij} = 2\rho\nu S_{ij}$ the viscous stress, $S_{ij} = \frac{1}{2}(u_{i,j} + u_{j,i})$ the resolved strain rate tensor, and τ_{ij}^{sps} the subparticle scale stress tensor calculated based on the eddy viscosity methodology.

Finally, p is the filtered pressure defined from the equation of state that relates the pressure in the fluid to the local fluid density, as given by Monaghan (1994):

$$p = B\left[\left(\frac{\rho}{\rho_0}\right)^\beta - 1\right], \tag{4}$$

where ρ_0 is the initial fluid density, $\beta = 7$ is a constant, $B = \rho_0 c_{s0}^2/\beta$, and c_{s0} is the speed of sound in the water, a value averaged over fluctuations due to temperature, pressure, and salinity, all conditions expected to vary with depth. As discussed by Monaghan (1994), c_{s0} needs to be at least 10 times the maximum particle velocity

in the domain to keep the changes in fluid density below 1%; however, we found that, for bed motions with large vertical accelerations (on the order of one g), we needed to use a larger (more realistic) value of $c_{s0} = 1,500$ m/s to avoid an overprediction of free surface elevations.

2.2. Model Setup

As described in Figure 1, our numerical experiments are performed in a virtual wave tank featuring an ocean of unperturbed depth h, in which we consider a vertically moving source of half-length b_0 (along the direction x) with three different shapes, including flush (frame a) and emerged (frame b) pistons and a piston with a trapezoid on its top (frame c). In the latter, a sill of half-length b_s and height $(h - h_s)$ is connected to the moving bed with a slope $1/s$. The original height of an emerged piston, which is a sill with vertical edges ($s = 0$) that occupies the entire source area, is $h - h_s$. The tank extends a length $\pm L_x/2$ in the x direction, and $\pm L_y/2$ in the transverse y direction. In practice, we consider a narrow tank ($L_y \approx 0.003 L_x$).

The vertical motion of the moving bed is imposed as $\zeta(x, t) = \xi(t) H(b_0^2 - x^2)$, where H is the Heaviside step function. Thus, the instantaneous elevation of the bed reads as $z_b(x, t) = z_b(x, 0) + \zeta(x, t)$. In this study, the function ξ is taken as follows:

$$
\begin{aligned}
\xi(t) &= 0 & t &< 0 \\
\xi(t) &= \frac{1}{2} \xi_m \left[1 - \cos \frac{\pi t}{t_r} \right] & 0 &\leq t \leq t_r \\
\xi(t) &= \xi_m & t &> t_r
\end{aligned}
\tag{5}
$$

where ξ_m is the maximum vertical displacement of the source. This choice of ξ has been used in a number of previous studies (e.g., Hammack, 1973; Jamin et al., 2015; Nosov & Kolesov, 2007). It has the property that the vertical velocity $\mathcal{W}$ of the moving bed remains continuous with time, increasing from $\mathcal{W} = 0$ for $t = 0$ to a maximum value $\mathcal{W}_m = \pi \xi_m / 2 t_r$ for $t = t_0 = t_r/2$ and then decreasing back to 0 at $t = t_r$. By contrast the acceleration a jumps to its maximum value $a_m = \pi^2 \xi_m / 2 t_r^2$ upon initiation of the motion ($t = 0$) and then decreases continuously to $-a_m$, when it terminates abruptly at $t = t_r$. Temporal variations of ξ, $\mathcal{W}$, and a are shown in Figures 1d–1f.

Each numerical scenario is defined by setting the geometry of the moving bed through the parameter b_0 and of the sill through the additional dimensions h_s and b_s and inverse slope s. In addition, we select the parameters ξ_m and t_r in (5) (or equivalently, ξ_m and a_m). In all cases, the depth of the unperturbed ocean, h, is taken as 200 m. A total number of 47 different scenarios is considered, with all relevant parameters compiled in Table 1.

As discussed above, t_c in equation (1) is the time it takes for a long wave to transit over half of the moving bed in a flat ocean of depth h, corresponding to $h_s = h$. In real cases for which $h_s < h$, it would take longer for the elevated water to flow out of the source region. In this context, we introduce the additional dimensionless variable

$$
\tau_s = \frac{t_r}{b_0 / \sqrt{g h_s}} = \tau \sqrt{\frac{h_s}{h}},
\tag{6}
$$

where

$$
\overline{h_s} = b_0^{-1} \int_0^{b_0} -z_b(x, 0) \mathrm{d}x = h - \frac{b_s}{b_0}(h - h_s) - \frac{1}{2} \frac{s(h - h_s)^2}{b_0}
\tag{7}
$$

is the average depth over the source. In cases with $s = 0$ (infinite sill slope), the initial bed elevations have a step-like discontinuity at the edge of the sill ($x = \pm b_s$). The range of parameters considered in our scenarios correspond to $0.08 < \tau < 88$, and in the presence of a sill, $0.04 < \tau_s < 88$.

All model simulations are performed with the model initialized with quiescent conditions. A periodic boundary condition is applied to the two lateral boundaries in the y direction. The moving particles at the bed are handled the same manner as those at fixed boundaries, except their instantaneous displacements are prescribed using equation (5). The two boundaries at $x = \pm L_x/2$, where L_x is the length of the computational domain in the x direction, are filled with fixed boundary particles, but in practice, all analyses of our computations are terminated before the waves reach the far-field boundaries ($t < (L_x/2)/\sqrt{gh}$).

Table 1
Input Parameters for the Simulated Cases

Case no.	h (m)	b_0/h	b_s/b_0	h_s/h	s	ξ_m/h	a_m/g	τ	τ_s
A1	200	10.0	1.00	1.0	0.0	0.10	0.81	0.08	0.08
A2	200	10.0	0.96	0.6	1.0	0.10	0.81	0.08	0.06
A3	200	10.0	0.94	0.4	1.0	0.10	0.81	0.08	0.05
A4a	200	10.0	1.00	0.3	0.0	0.10	0.81	0.08	0.04
A4b	200	10.0	0.93	0.3	1.0	0.10	0.81	0.08	0.04
A4c	200	10.0	0.80	0.3	1.0	0.10	0.81	0.08	0.05
A4d	200	10.0	0.70	0.3	1.0	0.10	0.81	0.08	0.05
A4e	200	10.0	0.50	0.3	1.0	0.10	0.81	0.08	0.06
A4f	200	10.0	0.25	0.3	1.0	0.10	0.81	0.08	0.07
A5	200	10.0	0.92	0.2	1.0	0.10	0.81	0.08	0.04
B1	200	5.0	1.00	1.0	0.0	0.10	0.81	0.16	0.16
B2	200	5.0	1.00	0.6	0.0	0.10	0.81	0.16	0.12
B3a	200	5.0	1.00	0.4	0.0	0.10	0.81	0.16	0.10
B3b	200	5.0	0.88	0.4	1.0	0.10	0.81	0.16	0.10
B3c	200	5.0	0.70	0.4	1.0	0.10	0.81	0.16	0.11
B3d	200	5.0	0.50	0.4	1.0	0.10	0.81	0.16	0.13
B3e	200	5.0	0.25	0.4	1.0	0.10	0.81	0.16	0.14
B3f	200	5.0	0.40	0.4	5.0	0.10	0.81	0.16	0.12
B4	200	5.0	1.00	0.3	0.0	0.10	0.81	0.16	0.09
B5a	200	5.0	1.00	0.2	0.0	0.05	0.81	0.11	0.05
B5b	200	5.0	1.00	0.2	0.0	0.10	0.81	0.16	0.07
B5c	200	5.0	0.84	0.2	1.0	0.10	0.81	0.16	0.08
B5d	200	5.0	0.67	0.2	1.0	0.10	0.81	0.16	0.10
B5e	200	5.0	0.50	0.2	1.0	0.10	0.81	0.16	0.11
B5f	200	5.0	0.25	0.2	1.0	0.10	0.81	0.16	0.13
B5g	200	5.0	0.50	0.2	3.0	0.10	0.81	0.16	0.10
B5h	200	5.0	0.20	0.2	5.0	0.10	0.81	0.16	0.11
C1–C3	200	5.0	1.00	1.0, 0.4, 0.2	0.0	0.10	0.081	0.5	0.5–0.2
D1–D3	200	5.0	1.00	1.0, 0.4, 0.2	0.0	0.10	0.020	1.0	1.0–0.4
E1–E4	200	5.0	1.00	1.0, 0.6, 0.4, 0.2	0.0	0.10	0.005	2.0	2.0–0.9
F1–F4	200	2.0	1.00	1.0, 0.6, 0.4, 0.2	0.0	0.10	0.005	5.0	5.0–2.2
G1, G2	200	1.0	1.00	1.0, 0.2	0.0	0.05	0.0025	10.0	10.0,4.5
H1, H2	200	1.0	1.00	1.0, 0.2	0.0	0.05	0.0005	22.0	22.0,9.8
I1, I2	200	0.25	1.00	1.0, 0.2	0.0	0.05	0.0005	88.0	88.0,39.4

Note. Here, h is the constant ocean depth, b_0, h_s, b_s, and s are defined in the top panels of Figure 1, ξ_m and a_m are the maximum vertical displacement and acceleration of the source respectively, t_r is the bed rise time, $\tau = t_r\sqrt{gh}/b_0$, and $\tau_s = t_r\sqrt{gh_s}/b_0$ (equations (6) and (7)).

The initial particle spacing for most cases is $\Delta = 0.02h$. This results in 50 particles distributed over the depth at the constant-depth region. In section 3, we show that decreasing the initial particle spacing Δ from $0.02h$ to $0.01h$ has a negligible effect on the results predicted in the current simulations, suggesting that the numerical error associated with the selection of grid size is also negligible.

2.3. The Interpolation Scheme

The Lagrangian model results are available at SPH nodes (or particles) that are distributed irregularly in space as they move with the fluid. To examine the Eulerian velocity and pressure fields, we need to map the SPH results onto an Eulerian grid. In this paper, we interpolated the Eulerian field ψ at a location **x** and time t from the corresponding simulated Lagrangian field at the neighboring SPH nodes ψ_a using the SPH
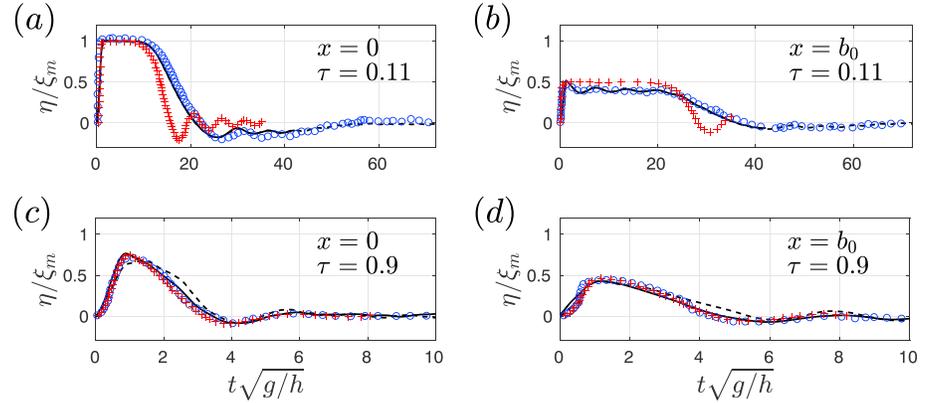
Figure 2. Hammack (1973) experimental data (circles) and analytical solutions (pluses) compared to GPUSPH results for the temporal variation of the normalized free surface elevations at (a, c) the center ($x/b_0 = 0$) and (b, d) edge ($x/b_0 = 1$) of the piston-like source for the (a, b) impulsive ($\tau = 0.11$, $\xi_m/h = 0.4$) and (c, d) transitional ($\tau = 0.9$, $\xi_m/h = 0.01$) bed displacement scenarios. Two different initial particle spacings are used: $\Delta = 0.01h$ (solid lines) and $\Delta = 0.02h$ (dashed lines).

interpolation kernel W at a given time:

$$\psi(\mathbf{x}) = \frac{\sum\limits_a \frac{m_a}{\rho_a} W(\mathbf{x} - \mathbf{x}_a, h_{sl}) \psi_a}{\sum\limits_a \frac{m_a}{\rho_a} W(\mathbf{x} - \mathbf{x}_a, h_{sl})}, \tag{8}$$

where m is the (constant) particle mass and subscript a refers to the particles within the influence volume of the interpolation kernel around the location $\mathbf{x}$ at time t. Here, the influence volume is taken as a sphere with a radius $2h_{sl}$. The Eulerian grid has a uniform grid size equal to the initial particle spacing Δ. Hereafter, all the equations and analyses are presented in the Eulerian form.

3. Uplift of a Flush Piston (No Sill): Inertia Effects

3.1. Model Validation

GPUSPH has been extensively validated and used for study of a number of wave-driven nearshore processes (Farahani & Dalrymple, 2014; Wei et al., 2017). In this section, we present the model validation for the generation of a wave by the uplift of a piston-like source in an otherwise constant-depth narrow tank using the experimental data of Hammack (1973). He made experimental observations of the free surface elevations η of the waves generated by a vertically moving flat bed section, which we call a flush piston (Figure 1a), with a half-length b_0 for two specific idealized bed deformation scenarios, a half-sine rise (ξ as given by (5) in the present study), and an exponential rise extending (at least conceptually) over an infinite time. The only measurements of the free surface available in Hammack (1973) are at the center ($x = 0$) and at the edge ($x = b_0$) of the moving bed. He also derived analytical solutions for the water surface displacement based on the linearized Euler equations.

Results of our computations are presented in Figure 2 as time series of normalized η at the center ($x = 0$; left frames) and edge ($x = b_0$; right frames) of the source, for impulsive scenarios ($\tau = 0.11$; $\xi_m/h = 0.4$; top frames) and transitional ones ($\tau = 0.90$, $\xi_m/h = 0.01$; bottom). They are compared with Hammack (1973) experimental data (blue circles) and linear analytical solutions (red plus signs). We note that the solid lines (GPUSPH with the initial particle spacing of $\Delta = 0.01h$) fit Hammack (1973) experimental data set with a high degree of accuracy and generally better than does his analytical solution, especially for longer times in the impulsive regime (Figures 2a and 2b). The only exception is a slight misfit at the edge of the uplifted bed at very short normalized times in the transitional regime (Figure 2d). When a larger Δ is used (resolution coarser by a factor of two, dashed lines), the maximum uplift at $x = 0$ is slightly underpredicted and the uplifted fluid remains too long over the uplifted bottom.

Note that in Figure 2b for the impulsive case, the water surface displacement at the edge of the uplift region remains nearly half the bottom displacement for a long time ($t \approx 25\sqrt{h/g}$). This can be explained by comparing this tsunami problem to a dam break problem, which also features the water depth remaining at 4/9 the
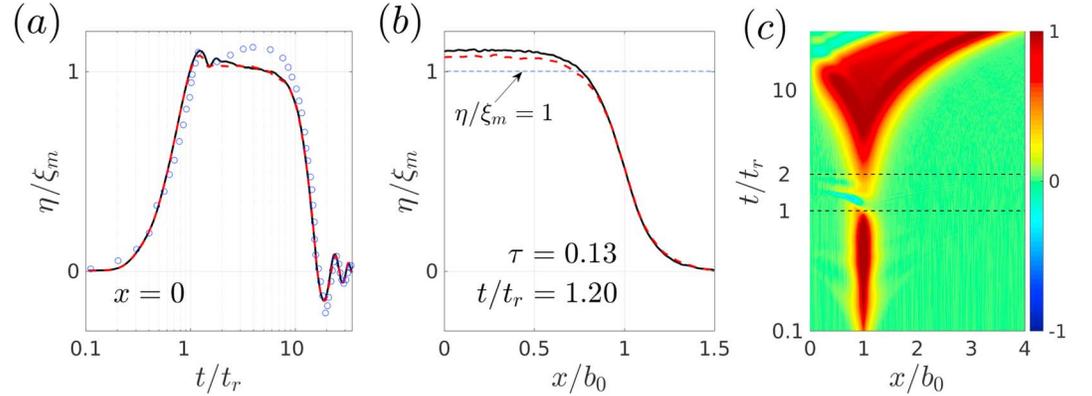
Figure 3. (a) Temporal and (b) spatial variation of the normalized free surface elevations at $x = 0$ and $t = 1.2\,t_r$ respectively, and (c) spatiotemporal variation of the normalized horizontal volume flux $q(x, t)$ defined in equation (10) for the impulsive bed displacement scenario with $\tau = 0.13$. Various lines in (a) and (b) represent the results of the present model with initial particle spacing of (solid lines) $\Delta = 0.01h$ and (dashed red lines) $\Delta = 0.02h$. Circles in (a) are the experimental data by Hammack (1973). Here, $b_0/h = 6.1$, $\xi_m/h = 0.1$, and t_r is the bed rise time.

initial depth at the dam for a considerable time (Stoker, 1957). Furthermore, as shown in Figures 2c and 2d, the model is able to predict the amplitude of waves generated at the surface for bed displacements less than the model particle size, here $\Delta = 2.0\xi_m$. The misfit between Hammack (1973) analytical and experimental data in frames (a) and (b) is traceable to the effect of nonlinearity: The parameter $\xi_m/h = 0.01$ in scenarios (c) and (d) implies weak nonlinearity, and thus, the linear solution captures the flow dynamics well.

Hereafter, we assess the GPUSPH's performance using the statistical method developed by Willmott (1981) for model predictive skill:

$$\text{Skill} = 1 - \frac{\displaystyle\sum_{i=1}^{N}|\psi_{i,\text{sim}} - \psi_{i,\text{obs}}|^2}{\displaystyle\sum_{i=1}^{N}\left[|\psi_{i,\text{sim}} - \bar{\psi}_{\text{obs}}| + |\psi_{i,\text{obs}} - \bar{\psi}_{\text{obs}}|\right]^2}, \tag{9}$$

where ψ is the variable being assessed, $\bar{\psi}$ is its sample mean value, and subscripts $()_{\text{sim}}$ and $()_{\text{obs}}$ stand for the simulated results (GPUSPH output) and observations (experimental data from Hammack, 1973), respectively. This skill parameter measures the degree to which the observed deviations about their mean correspond with the simulated deviations about the same mean. Perfect agreement between the simulated results and observations yields a skill of 1.0, whereas complete disagreement yields a skill of 0 (Willmott, 1981). Here, we examine the model predictive skill for the free surface elevations at $x = 0$ and b_0, where we have experimental data. Thus, at each particular location, x^*, we have $\psi_i = \eta(x^*, t_i = i\,dt)$, where $i = 1, 2, 3, \ldots, N$. Our model's predictive skills for $\eta(x^*, t)$ are above 0.99 and 0.96 for the impulsive and transitional scenarios in Figure 2, respectively. These high values establish the validity of the numerical model for this problem.

3.2. Inertia Effects

In Figure 3 we examine in more detail another impulsive scenario ($\tau = 0.13$) for which the model predictive skill remains very high (>0.98). We also confirm that the predicted results are not sensitive to the initial particle spacing for $\Delta < \xi_m/4$.

Interestingly, Figure 3a also demonstrates that the free surface displacement at $x = 0$ rises to its maximum at a time on the order of t_r and remains slightly greater than ξ_m for a significant time even after the bed displacement has stopped (note the logarithmic scale of the time axis). This is due to the inertia of the water mass displaced above the moving bed. This oscillation is strongly damped and in both the linear analysis of Hammack and the SPH model, the free surface stabilizes for a short time (until $t/t_r = 6$). Then the water level begins to fall; it takes a normalized time on the order of $1/\tau$ (i.e., a physical time on the order of t_c) for the displaced water to flow out of the source region and hence for η to fall to 0. Figure 3b, a snapshot of the free surface at $t/t_r = 1.2$, that is, slightly after the moving bed has stopped, documents the presence of an
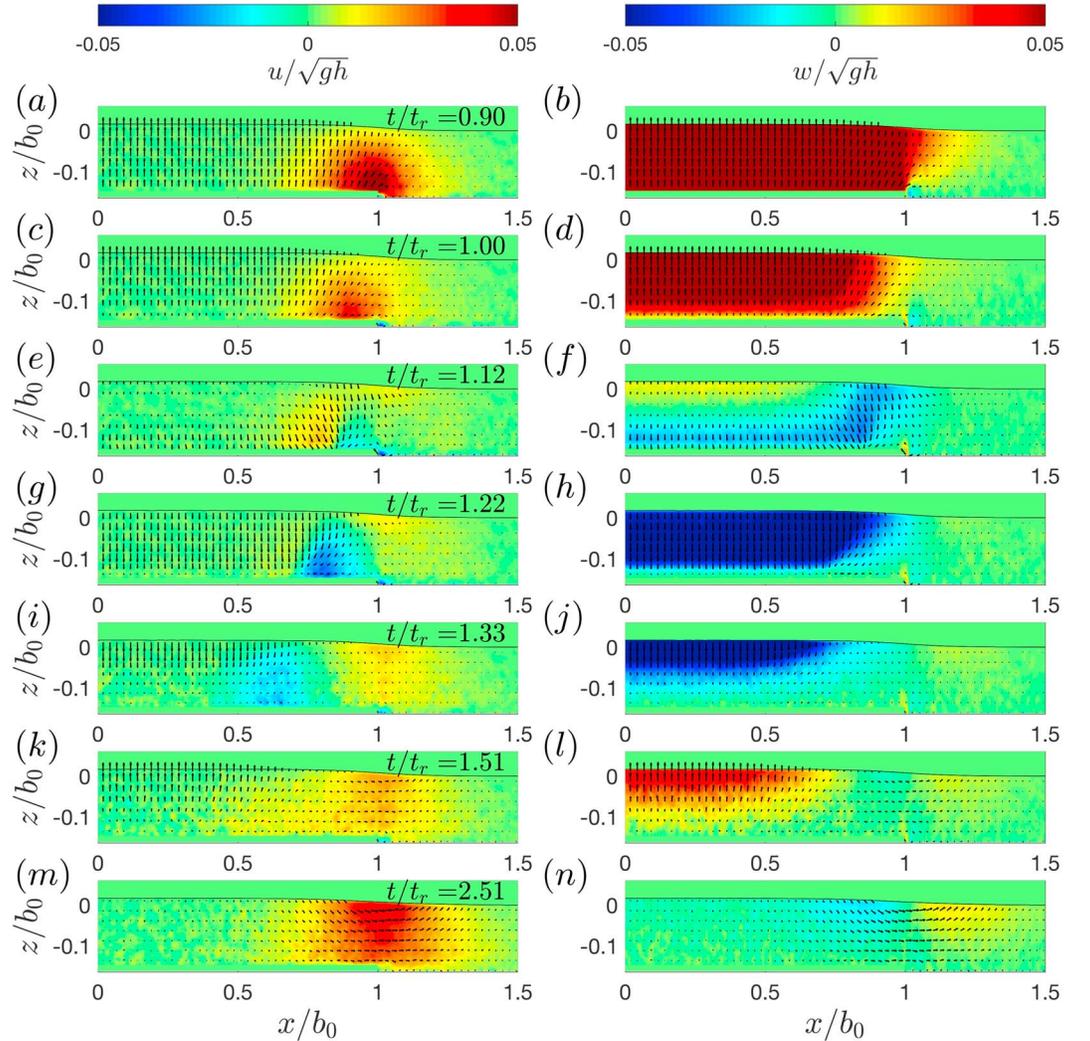
Figure 4. Snapshots of the spatial distribution of the normalized (a, c, e, g, i, k, and m) horizontal and (b, d, f, h, j, l, and n) vertical velocity for the impulsive bed displacement scenario with $\tau = 0.13$ shown in Figure 3. Due to the inertia of the upward moving water mass over the uplifting bed section, maximum free surface elevation occurs after the bed rise time at $t/t_r \sim 1.15$.

overshoot ($\eta/\xi_m - 1 \approx 10\%$), occurring across a broad portion of the source area (except of course close to its edge, $x/b_o \geq 0.8$, where the water has already drained into the deeper basin). This predicted overshoot is generally consistent with Hammack's experimental observations for $1 \leq t/t_r \leq 2$, but this interesting phenomenon was not mentioned by that author nor to our knowledge by any of the relevant subsequent studies. Its properties and consequences will be examined more in detail in a future study.

Figure 3c further contours the normalized depth-integrated volume flux in the x direction per unit width, $q(x, t)$, given by

$$q(x, t) = \frac{2}{L_y \xi_m \sqrt{gh}} \int_{-L_y/2}^{L_y/2} \int_{z_b}^{\eta} u(x, y, z, t) \mathrm{d}z \mathrm{d}y, \quad (10)$$

where L_y is the domain length in the transverse direction and $0.5\xi_m\sqrt{gh}$ is the reference flux value per unit length, which is equal to an outward flux at the edge of the source assuming linear long wave theory. The flux q may be also interpreted as the distribution of the horizontal momentum in the near field. Assuming no cavitation, the overshoot can only occur if the water flows toward the center of the moving bed to conserve the total water mass. Indeed, Figure 3c confirms this phenomenon by showing a negative flux (blue streak) occurring at the edge of the source (x slightly less than b_0) for $1 < t/t_r < 1.5$. Note in particular the negative
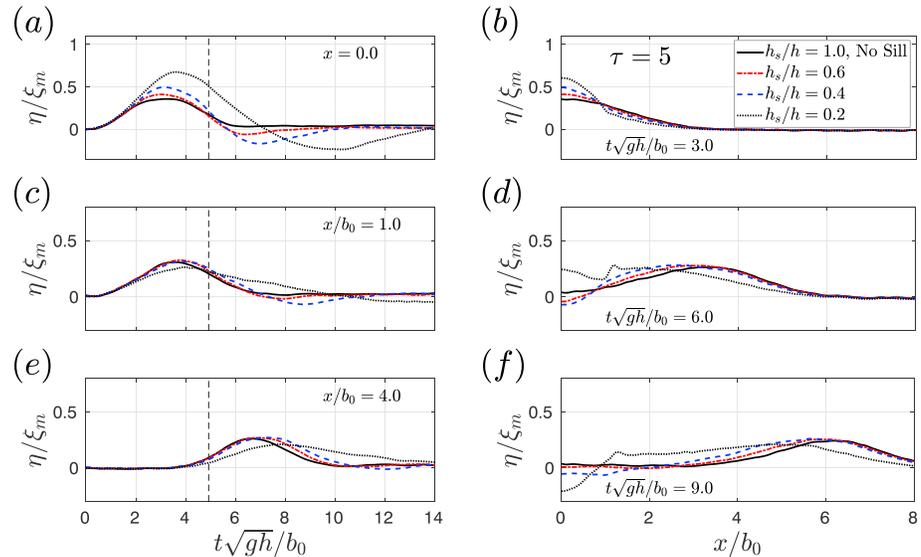
Figure 5. Variation of the wavefield generated at the surface with normalized sill height $(h - h_s)/h$ for the creeping bed displacement scenario with $\tau = 5$. Temporal (a, c, and e) and spatial (b, d, and f) variation of the normalized free surface elevations at various locations x and times t. Here, the sill has an emerged piston shape shown in Figure 1b. Note that $\tau = t_r/t_c$, where $t_c = \sqrt{gh}/b_0$, and thus, vertical dashed lines represent the physical time of $t = t_r$ and nondimensional time of τ.

slope of the blue streak on Figure 3c, which illustrates the inward flux of water toward the center of the source.

Figure 4 shows snapshots of the spatial evolution of horizontal and vertical components of the velocity field normalized by $\sqrt{gh}$ in the x-z plane between $t/t_r = 0.9$, that is, slightly before the moving bed has stopped, and $t/t_r = 2.51$. The evolution of the horizontal velocity (left frames) demonstrates that at $t/t_r = 1.12$ an inward flow is first developed near the edge of the source, and then the height of its velocity front becomes greater as it propagates toward the center of the source. Further, the evolution of the vertical velocity for $1 < t/t_r < 2.51$ (right frames) shows that the displaced water that was originally driven upward by the source reverses sign and then rebounds to an upward velocity over a large portion of the source area. Comparing the x location of the inward front shown in Figures 4g and 4i, or calculating the slope of the blue streak in Figure 3c, implies a speed of $\sim 1{,}000$ m/s for the inward flowing front. This implies that this mass transfer front constitutes neither a tsunami-like gravity wave (which would be much slower) nor a hydroacoustic phenomenon, which would be propagating faster at 1,500 m/s. At later times, for example, $t/t_r = 2.51$ (frames m and n), the velocity field becomes consistent with that of a long wave radiating away from the source region into the far field.

4. Adding a Sill to the Source Region

4.1. An Emerged Piston

We now add to our source region a sill, rising to a height $h - h_s$ over the entire source area, that is, a geometry that prior to the uplift the otherwise flat bottom has a rectangular mound over the entire source area (Figure 1b). We examine η as a function of both x and t, for different sill heights for a creeping scenario ($\tau = 5$; Figure 5) and an impulsive one ($\tau = 0.16$; Figure 6). In each case, the left frames (a, c, and e) show the temporal variation of η at the center of the source ($x = 0$), at its edge ($x/b_0 = 1$), and far beyond it ($x/b_0 = 4$), respectively. Similarly the right frames (b, d, and f) show snapshots of its spatial variation for a number of times. Frame (e) of Figures 5 and 6 documents that an increase of sill height (or a decrease of h_s/h) generally decreases the height of the leading wave in the far field, while its dominant period increases. Further, Figure 7 shows that the outflow from the source $q(x = b_0, t)$ has a relatively small magnitude but a longer time scale as h_s/h decreases. This is consistent with the results on the height and dominant period of the radiated wave. Not surprisingly, this also explains the increase of the maximum trough elevation, as shown in frame (a) of Figures 5 and 6, with the decrease of h_s/h.
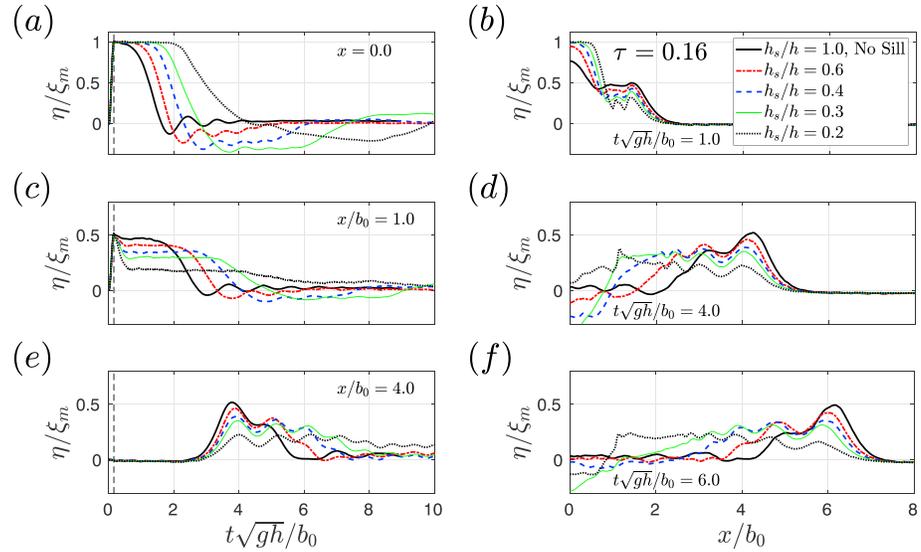
Figure 6. Same as in the Figure 5 except for the impulsive bed displacement scenarios with $\tau = 0.16$.

In the impulsive case with $h_s/h = 0.2$ (Figure 6, dotted lines), the decrease of the height of the leading wave in the far field is quite significant and the radiated wave has a different spatial structure. This is due to the formation of a feature similar to a hydraulic jump just offshore of the edge of the sill. Further, as the sill's height increases, the leading wave seems to have more pronounced dispersive behavior, as compared with the corresponding case with no sill. In the creeping case (Figure 5), varying the height of the sill has a similar trend on the radiated wave, but its effect is much weaker, compared with the impulsive case.

In both of the figures, the near-field waves that radiate away from the source do not have significant troughs as fluid is flowing out of the source area. As the waves propagate further away, soliton fissioning begins to occur. Both of these effects are due to the fact that the initial displacement of the water surface, which when integrated in space, yields a positive value, as explained by Hammack and Segur (1974).
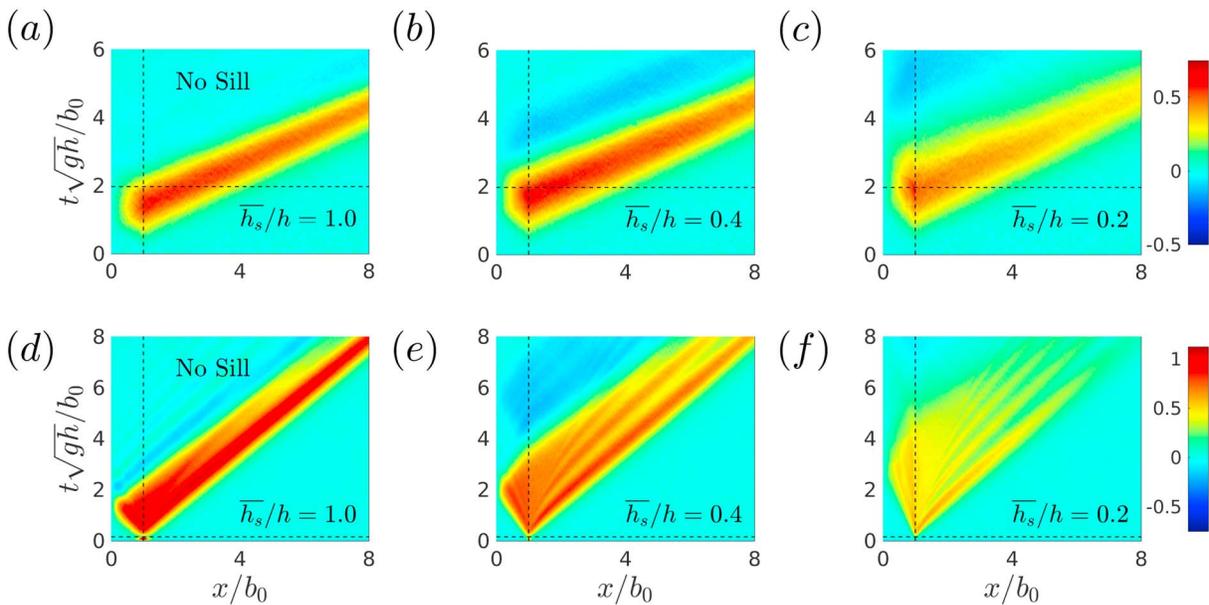
Figure 7. Spatiotemporal variation of the normalized horizontal volume flux $q(x, t)$ defined in equation (10) for the (a–c) creeping ($\tau = 5$) and (d–f) impulsive ($\tau = 0.16$) bed displacement scenarios with various averaged sill heights ($1-\overline{h_s}/h$). Here, the sill has an emerged piston shape shown in Figure 1b, and thus, $\overline{h_s} = h_s$. The horizontal and vertical dashed lines in each panel represent $t = t_r$ and $x = b_0$, respectively.
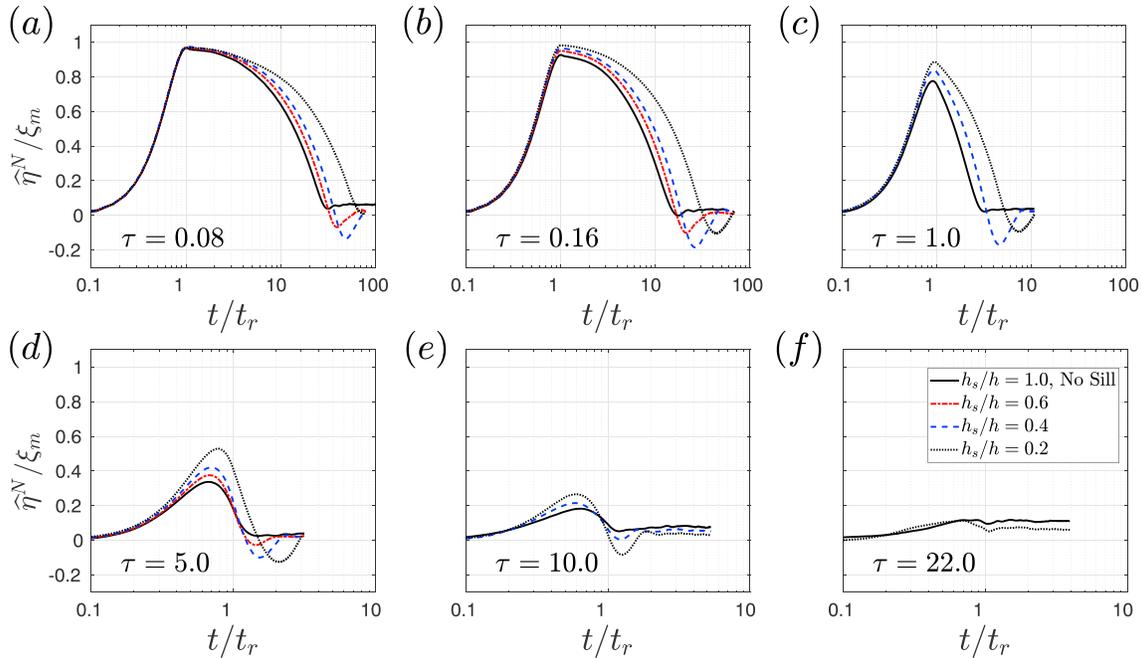
Figure 8. Temporal variation of the normalized spatial-averaged free surface elevation of the wave generated over the moving bed region, $\hat{\eta}^N(t) = \frac{1}{b_0} \int_0^{b_0} \eta(x,t)dx$, with the normalized sill height $1 - h_s/h$ and nondimensional rise time τ. Here, the sill has an emerged piston shape shown in Figure 1b.

By contrast, the temporal variation of η at the center of the source ($x = 0$) has a different trend in the creeping case (Figure 5a), as compared with the impulsive one (Figure 6a). In the creeping case, $\eta(x = 0)$ increases to a maximum (smaller than ξ_m) at a time $t < t_r$ while for impulsive cases, the maximum value ($\approx \xi_m$) is reached at $t = t_r$. As shown in Figure 7, this simply expresses the fact that in creeping cases, the source is slow and a noticeable fraction of the displaced water flow away from the source before the end of the rise, that is, $\int_0^{t_r} q(b_0,t)dt / \int_0^\infty q(b_0,t)dt \sim O(1)$; as a consequence, the maximum value of η is significantly reduced. Furthermore, Figure 5a shows that in creeping cases, the maximum amplitude $\eta(x = 0)$ increases with decreasing h_s, since the water that is not moved efficiently out of the source region in the presence of the sill, must then rise with it, that is, $\int_0^{t_r} q(b_0,t)dt$ is a decreasing function of the sill height as shown in the top frames of Figure 7. By contrast in the impulsive cases, and irrespective of the value of h_s/h, there is no time for the water to flow out; that is, $\int_0^{t_r} q(b_0,t)dt / \int_0^\infty q(b_0,t)dt \ll 1$ as shown in the bottom frames of Figure 7, and thus, $\eta_{\max} \approx \xi_m$.

In addition, note that in creeping cases (Figure 5a), the amplitude $\eta(x = 0)$ starts decreasing immediately after reaching its maximum, whereas in impulsive ones (Figure 6a), its decay is significantly delayed. This is due to the time necessary for the water to flow out of the source region, especially in the presence of a large sill (e.g., $h_s/h = 0.2$) reducing the "escape" velocity of the water over, and out of, the source area.

Finally, Figures 6d and 6f, away from the source area ($x/b_0 > 4.0$), show that the leading wave is larger when h_s/h is larger. Similarly, Figure 7 shows that the outward flux is larger when the sill is smaller. This simply reflects the fact that the more water is moved over the source area, the larger the tsunami. It also reflects the fact that the smaller the sill, the smaller the contrast between source and basin depth and hence the weaker the faltering of the far-field wave in the sense of Green (1837) law.

To further examine the variation with h_s and τ of the wavefield generated at the surface of the source region, we define the instantaneous spatial average of η over it:

$$\hat{\eta}^N(t) = \frac{1}{b_0} \int_0^{b_0} \eta(x,t)dx. \qquad (11)$$

The results, presented in Figure 8, generalize the conclusions of Figures 5a, 5b, 6a, and 6b (note the abscissa is logarithmic in t): Under the impulsive scenario (Figures 8a and 8b), the maximum average amplitude $\hat{\eta}^N_{\max}$ remains close to ξ_m and is reached at $t \approx t_r$; the amplitude then decreases relatively slowly, the more
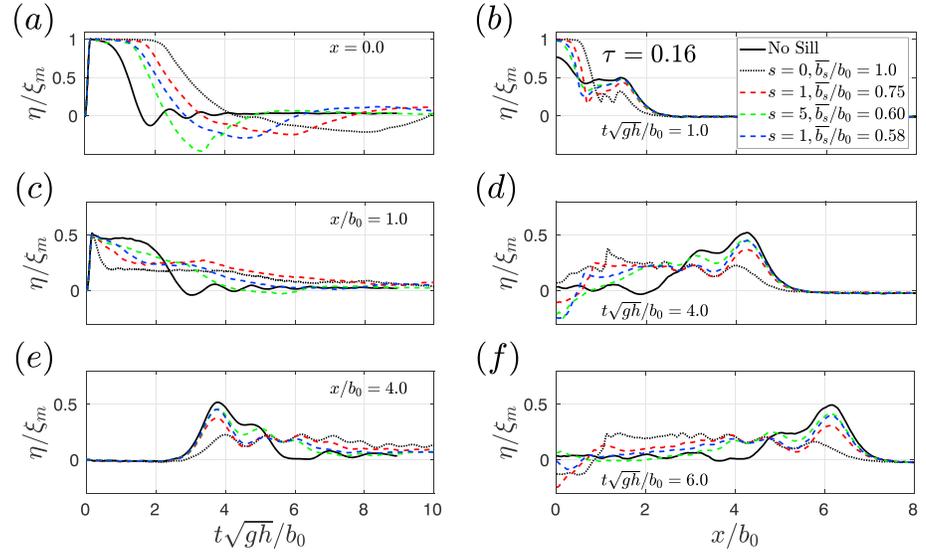
Figure 9. Effects of the relative averaged width of the sill $b_s^* = \overline{b_s}/b_0$ defined in (12) with $h_s/h = 0.2$ on the wavefield generated at the surface. Temporal (a, c, and e) and spatial (b, d, and f) variation of the normalized free surface elevations at various locations x and times t for the impulsive bed displacement scenario with $\tau = 0.16$. As shown in Figure 1c, in cases including a sill with $\overline{b_s}/b_0 < 1$ the sill of half-length b_s and height $(h - h_s)$, connected to the moving bed with a slope $1/s$.

so with increasing sill height and decreasing τ. By contrast, for creeping cases (Figures 8e and 8f), $\hat{\eta}_{\max}^N$ is sharply reduced, the effect becoming more severe with increasing τ but slower with increasing sill height; the maximum is reached before $t < t_r$, and the amplitude starts decreasing before the end of the rise.

4.2. A Piston With a Trapezoid on Top

In all previous cases, we had considered the case of a constant elevation sill occupying the entire source region ($b_s = b_0$ with $s = 0$, and thus, $\overline{h_s} = h_s$). We now consider the influence of the shape of the sill by varying the parameters b_s/b_0 (dimension of the top of the sill) and s (inverse slope). We further express the averaged size of the sill as

$$\overline{b_s} = b_s + s(h - h_s)/2 \tag{12}$$

and a dimensionless

$$b_s^* = \overline{b_s}/b_0, \tag{13}$$

which characterize the horizontal extent of the sill to the point where it reaches its half-height along its slope in the geometry of Figure 1c. In all cases, we use a tall sill ($h_s/h = 0.2$). Figure 9, for an impulsive bed displacement scenario, compares dimensionless free surface elevations for various values of b_s^* (0, 0.58, 0.60, 0.75, 1), with the extremes being no sill ($b_s^* = 0$) and the sill occupying the entire source area ($b_s^* = 1$). Our results show that decreasing b_s^* increases the height of the radiated leading wave, as there is more fluid over the uplift region at the outset, and that the difference between the height of the radiated leading wave in cases with different lateral slope $1/s$ but with the same b_s^* is relatively small. This suggests that b_s^* is a robust parameter controlling the combined effects of sill width (b_s) and slope ($1/s$) on the radiated leading wave in the far field.

4.3. Summary of Results and Proposed Parameterization

The influence of the parameters of the source, and specifically of the presence of the sill, is further explored by focusing on three measures of their effect. First, we consider the ratio η_m^0/ξ_m, the maximum wave amplitude at the center of the source ($x = 0$) to the maximum vertical displacement of the bottom. Next, we define a similar ratio for the source-averaged $\hat{\eta}^N$ defined in equation (11). These two metrics characterize the sensitivity of the wavefield in the source region to the characteristics of the bed deformation. Finally, we envision
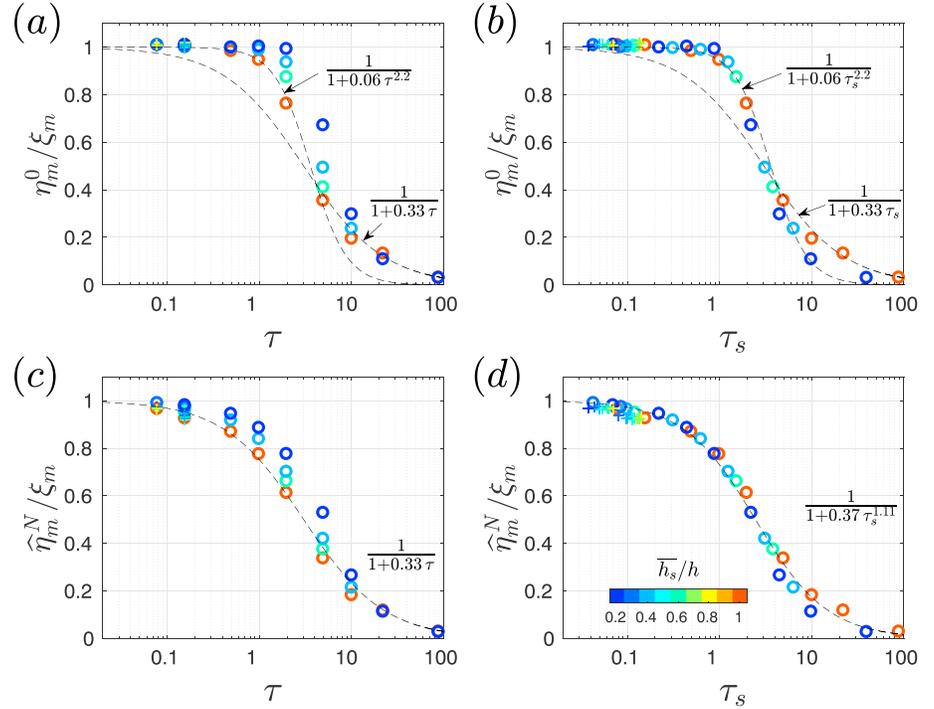
Figure 10. Variation of the normalized (a, b) maximum crest elevation at the center of the source $x = 0$ and (c, d) maximum spatial-averaged η over the source region, for all cases, with nondimensional rise times (a, c) τ and (b, d) τ_s, defined in equation (6). Here, ξ_m is the maximum vertical displacement of the moving bed. Circles and pluses refer to cases with $b_s *= 1$ and $b_s^* < 1$ respectively. Colors indicate the ratio $\overline{h_s}/h$.

a "far-field" point F located significantly outside the source region, at a distance x^F, which we take as at least three source sizes b_0 (but not greater than 15 depths h) beyond the edge of the source:

$$x^F = b_0 + \text{Min}(3b_0, 15h) \tag{14}$$

and define the ratio η_m^F/ξ_m, which characterizes how sensitive the radiated wave in the far field is to the parameters of the source.

In general terms, the various models have three independent degrees of freedom: the parameter τ (equation (1)) controlling the nature (impulsive, transitional, or creeping) of the scenario, the nondimensional ratio $\overline{h_s}/h$ (equation (7)) characterizing the relative height of the sill, and the nondimensional parameter b_s^* (equation (13)) characterizing the lateral extent of the sill across the source.

Figure 10 examines the variation of η_m^0/ξ_m and $\hat{\eta}_m^N/\xi_m$ for various rise times and sill geometries. In the left frames, the variation of these parameters with τ is shown. The η_m^0/ξ_m values corresponding to cases with $\overline{h_s}/h = 1$, the cases with no sill in the source region, are consistent with the previous studies (e.g., Hammack, 1973). Figure 10a shows that the effect of varying sill height (or $\overline{h_s}/h$) on η_m^0/ξ_m is only noticeable for the cases with $1 < \tau < 10$, and Figure 10b shows that η_m^0/ξ_m is then a decreasing function of τ_s for this range of bed scenarios. Figures 10c and 10d show that the variation of $\hat{\eta}_m^N/\xi_m$ with τ and τ_s has a similar trend as for η_m^0/ξ_m, where the effect of sill height on the former remains noticeable down to the cases with $\tau \approx 0.1$. For the cases with $\tau > 10$, η_m^0/ξ_m and $\hat{\eta}_m^N/\xi_m$ are simply decreasing with decreasing τ irrespective of the value of $\overline{h_s}/h$. Based on the fitted lines shown in Figure 10, we may write

$$\frac{\eta_m^0}{\xi_m} = \frac{1}{1 + 0.06\ \tau_s^{2.2}}, \qquad \tau < 10, \tag{15}$$

$$\frac{\eta_m^N}{\xi_m} = \frac{1}{1 + 0.37\ \tau_s^{1.11}}, \qquad \tau < 10, \tag{16}$$
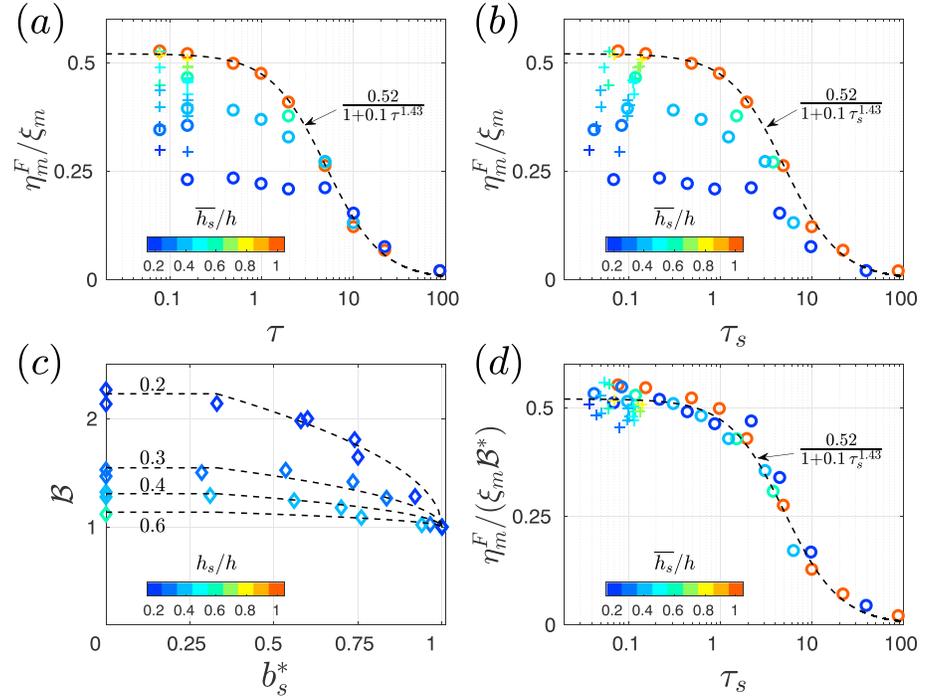
Figure 11. (a, b, and d) Variation of normalized maximum crest elevations of the radiated leading wave in the far field at $x = x^F$ (equation (14)) with τ and τ_s for all cases and (c) sensitivity of $\mathcal{B}$ defined in equation (19) with the normalized averaged width of the sill $b_s^* = \overline{b}_s / b_0$ for impulsive cases. Dashed lines in (c) show $\mathcal{B}$ for various values of $h_s/h = 0.2$, 0.3, 0.4, and 0.6. In (d), $\mathcal{B}^*$ is the transfer function, representing the effect of the geometry of the sill on η^F, and is defined in equation (21). In (a), (b), and (d), circles and pluses refer to cases with $b_s *= 1$ and $b_s^* < 1$, respectively.

and

$$\frac{\eta_m^0}{\xi_m} \approx \frac{\eta_m^N}{\xi_m} = \frac{1}{1 + 0.33\,\tau}, \qquad \tau \geq 10. \tag{17}$$

So far, we showed that both near-field measures η_m^0/ξ_m and $\hat{\eta}_m^N/\xi_m$ can be parameterized by simple relationships depending only on τ_s for $\tau < 10$ and on τ for $\tau \geq 10$. In other words, the effect of sill geometry on the near-field wave for creeping cases with $\tau \geq 10$ is relatively small. Further, our results show that varying the lateral extend and the shape of the sill, $0 < b^* < 1$, has a relatively small effect on the near-field wave and that the main factors determining the characteristics of the wavefield generated at the surface over the source are the total volume of water over the source $2b_0\overline{h}_s$, the total volume of the displaced water during the seabed dislocation $2b_0\xi_m$, and the rate at which the volume $2b_0\xi_m$ is displaced. We will comment on the application of these results (equations (15) to (17)) in the case of nonuniform source displacement in the following section.

By contrast, Figures 11a and 11b show that the amplitude in the far field, illustrated by the parameter η_m^F/ξ_m, is strongly sensitive to the lateral extend and shape of the sill and that the presence of a sill could decrease the height of the radiated wave by more than 60% compared with the case without a sill. Further, the results indicate that we need to have a transfer function $\mathcal{B}^* = \mathcal{B}^*(h_s/h, b_s^*, \dots)$ incorporating both the lateral extend and shape of the sill in addition to τ_s. We note that the values corresponding to cases with $\overline{h}_s/h = 1$, the cases with no sill in the source region, are consistent with the previous studies (e.g., Hammack, 1973), indicating that the maximum height of the wave radiated into the far field is approximately half of ξ_m for an impulsive motion.

We define the ratio $\mathcal{B}$ of the maximum wave amplitudes at x^F for a particular sill model to its value for a sill occupying the entire source region ($b_0^* = 1$):

$$\mathcal{B} = \frac{\eta_{\max}(x = x^F)}{\eta_{\max, b_s^*=1}(x = x^F)}. \tag{18}$$

where $\mathcal{B}(b^* = 0) = \eta^F_{m,\text{No Sill}}/\eta^F_{m,b^*_s=1}$ is the ratio of maximum wave amplitude at far field for a case without a sill to that with a sill with $b^*_s = 1$ and $\mathcal{B}(b^* = 1) = 1$. Figure 11c shows the sensitivity of $\mathcal{B}$ to b^*_s for the impulsive cases. Based on two-parameter nonlinear curve fitting, we obtain

$$\mathcal{B} = 1 + 0.06(h_s/h)^{-2}\left(1 - \text{Max}[b^*_s, 1/3]\right)^{0.5} \tag{19}$$

where $\mathcal{B}(b^* \leq 1/3) = \mathcal{B}(b^* = 0)$. In other words, the decrease of η^F_m due to a sill with $b^*_s \leq 1/3$ is found to be relatively small. Thus, we may write, based on (18) and (19),

$$\frac{\eta^F_m}{\xi_m} = \mathcal{B}\frac{\eta^F_{m,b^*_s=1}}{\xi_m} = \frac{\mathcal{B}}{\mathcal{B}(b^*_s = 0)}\frac{\eta^F_{m,\text{No Sill}}}{\xi_m} = \mathcal{B}^*\frac{\eta^F_{m,\text{No Sill}}}{\xi_m}, \tag{20}$$

where the transfer function $\mathcal{B}^*$ reads as

$$\mathcal{B}^*(h_s/h, b^*_s) = \frac{\mathcal{B}}{\mathcal{B}(b^*_s = 0)} = \frac{1 + 0.06(h_s/h)^{-2}\left(1 - \text{Max}[b^*_s, 1/3]\right)^{0.5}}{1 + 0.049(h_s/h)^{-2}}. \tag{21}$$

Figure 11d shows that using the scaling arguments discussed above successfully collapses the scatter of data due to the sill geometry observed in Figures 11a and 11b. Based on Figure 11d, we obtain a simple relationship to predict the normalized height of the radiated leading wave outside of the source region as a function of the relative height h_s/h and averaged width b^*_s of an idealized submerged sill (Figure 1) and of the nondimensional rise time τ_s:

$$\frac{\eta^F_m}{\xi_m} = \begin{cases} \dfrac{0.52}{1+0.1\tau_s^{1.43}}, & b^*_s < 1/3 \\[4mm] \dfrac{0.52}{1+0.1\tau_s^{1.43}}\left[\dfrac{1+0.06(h_s/h)^{-2}\left[1-b^*_s\right]^{0.5}}{1+0.049(h_s/h)^{-2}}\right], & b^*_s \geq 1/3. \end{cases} \tag{22}$$

5. Discussion: Relevance to Realistic Seismic Sources

So far we proposed simple scaling relationships (equations (15)–(17) and (22)) to predict the maximum height of the generated tsunami over and outside the source, in terms of parameters of the source ξ_m, $\tau = t_r\sqrt{gh}/b_0$, and of a submerged sill h_s, $\overline{h}_s$ and $\overline{b}_s$. Here, we comment on the application of our results to the case of realistic seismic sources.

As explained in section 2.2, we assumed that the vertical motion of the source $\zeta(x, t) = \xi(t)\phi(x)$ is uniform over the entire source area, $\phi(x) = H(b_0^2 - x^2)$, where H is the Heaviside step function. However, the final vertical displacement of the seabed is nonuniform over the source. In this case, we can define an effective half-width of an equivalent piston-like moving source b_0^{eff} as half of the ratio of the total volume of displaced water due to the source motion to the maximum vertical displacement of the source ξ_m; that is, $b_0^{\text{eff}} = \int_{-\infty}^{\infty}\zeta(x, t = t_r)\mathrm{d}x/2\xi_m$. As a first approximation, one may take $b_0 \approx b_0^{\text{eff}}$ to use in our scaling relationships described in section 4.3. However, the validity of such simplification needs to be examined.

In order to apply our results to the case of conventional seismic sources, we transcribe in the present notation our earlier result (Okal, 2003, equation A5) expressing the rise time t_r of the source as a function of fault length

$$t_r = A\frac{b_0}{\beta}, \tag{23}$$

where β is the shear velocity of the elastic medium and $A = \frac{16\sqrt{2}}{7\pi^{3/2}} \approx 0.58$ is a dimensionless constant; we recall that this formula was obtained using early work by Kanamori (1972) and assuming seismic scaling laws (Geller, 1976; Kanamori & Anderson, 1975). Substituting (23) into (1), we find

$$\tau = A\frac{\sqrt{gh}}{\beta}, \tag{24}$$

an extremely simple result that predicts that τ should be an invariant of the size of an elastic dislocation as long as the latter follows seismic scaling laws. Using a typical oceanic depth of $h = 4$ km in epicentral areas and a crustal shear velocity of 3.5 km/s, we obtain $\tau = 0.03$, in the impulsive regime.

By contrast, in the case of slow slip events (and notwithstanding their generally deeper location), their spatial extent of at most a few hundred kilometers would result in a time of transit t_c for any generated water wave of less than 2,000 s (even in shallow water), which combined with a source rise time of more than 1 day, leads to large values of τ, typically greater than 50.

In the case of very slow earthquakes, which may have rise times on the order of 200 s, τ could take an intermediate value on the order of 1, if their fault length reached ~50 km, which may be appropriate in the moment range of 10^{26} dyn.cm (Schwartz & Rokosky, 2007). For reference, in the case of interseismic creep mentioned in the Introduction, τ would reach extremely large values, on the order of 10^{10} to 10^{11}.

Finally, even for the case of a regular earthquake, the situation is made more complex by the spatial extent of the source over a finite fault length, which for mega-earthquakes can reach hundreds of kilometers (1,200 km for the 2004 Sumatra event; Ishii et al., 2005), the propagation of the rupture along the full fault zone defining a rupture time that reached up to 500 s in the case of the Sumatra event (Ni et al., 2005). This has the effect that the history of vertical deformation of the ocean bottom, $\xi(t)$, itself becomes a function of the abscissa y along the direction of rupture, a feature not considered in our models.

6. Conclusions

A smoothed particle hydrodynamic model GPUSPH was used to study the effects of the shape of the source on the dynamics of earthquake-generated tsunamis. We used an idealized geometry of the source region that included a flat section capped with a submerged sill. The model was validated against the experimental data of Hammack (1973) with high model predictive skills of more than 0.96 for the elevations of the generated free surface waves. The main conclusions are summarized as follows.

a. *Inertial effects*: We established that the maximum free surface displacement of the generated wave over the source for impulsive motions can be greater than the maximum vertical bed displacement ξ_m due to the inertia of the moving water. This overshoot occurs in a large portion of the generation region, with a time scale on the order of the bed rise time t_r. This overshoot is made possible by an inward volume flux of fluid toward the center of the source region to satisfy mass conservation, which is documented in Figures 3c and 4. Further, we observed an interesting inward flow feature that was developed near the source edge slightly after the bed has stopped and propagated toward the center of the source with a speed much faster than the tsunami speed but slower than the speed of sound in water.

b. *Effect of the nondimensional rise time τ*: We found that maximum heights of the leading wave in the far field in creeping cases $\tau \sim 10$ and $\tau \sim 100$ are lower than in impulsive cases $\tau \ll 1$ by a factor of 4 and 25, respectively. We conclude that a bed deformation scenario with $\tau > 100$ is not capable of tsunami genesis.

c. *Effect of the shape of a sill*: We found that an increase in the averaged height ($\bar{h}_s/h$) and width (b_s^*) of the sill systematically decreases the height of the leading wave into the far field, especially for an impulsive scenario, and by an amount of up to 60% compared with the case without a sill; this decrease was found to be relatively small if the averaged width of the sill is smaller than one third of the source size (or if $b_s^* < 1/3$). For cases with $1 < \tau < 10$, we conclude that the maximum height of the wave generated at the surface over the source is an increasing function of the total volume of water over the source region, while it is not sensitive to the lateral slope and width of the sill. Further, we found that the effect of a sill on the wavefield is relatively small for $\tau > 10$.

d. *Parameterization of tsunami height generated by a source including a sill*: We provided a series of simple forecasting tools in the form of parameterized relations that include rise time and source geometry and that quantify the difference between the variables η_m and ξ_m over, and outside of, the source.

In conclusion, this paper provides a quantification of the effects of the spatial and temporal characteristics of a bed deformation on the wavefield amplitudes over the source. As such, it puts constraints on the validity of the widely accepted practice of directly transposing the deformation of the bottom (ξ_m) to the free surface (η_m) and using it as an initial condition of a large-scale hydrodynamic simulation.

References

Beroza, G. C., & Ide, S. (2011). Slow earthquakes and nonvolcanic tremor. *Annual Review of Earth and Planetary Sciences*, *39*, 271–296.

Dalrymple, R. A., & Rogers, B. D. (2006). Numerical modeling of water waves with the SPH method. *Coastal Engineering*, *53*(2), 141–147.

Farahani, R. J., & Dalrymple, R. A. (2014). Three-dimensional reversed horseshoe vortex structures under broken solitary waves. *Coastal Engineering*, *91*, 261–279.

Geller, R. J. (1976). Scaling relations for earthquake source parameters and magnitudes. *Bulletin of the Seismological Society of America*, *66*, 1501–1523.

Gisler, G. R. (2008). Tsunami simulations. *Annual Review of Fluid Mechanics*, *40*, 71–90.

Glimsdal, S., Pedersen, G. K., Atakan, K., Harbitz, C. B., Langtangen, H. P., & Løvholt, F. (2006). Propagation of the Dec. 26, 2004, Indian Ocean Tsunami: Effects of dispersion and source characteristics. *International Journal of Fluid Mechanics Research*, *33*, 15–43.

Green, G. (1837). On the motion of waves in a variable canal of small depth and width. *Transactions of the Cambridge Philosophical Society*, *6*, 457.

Hammack, J. L. (1973). A note on tsunamis: Their generation and propagation in an ocean of uniform depth. *Journal of Fluid Mechanics*, *60*, 769–799.

Hammack, J. L., & Segur, H. (1974). The Korteweg-de Vries equation and water waves. Part 2. Comparison with experiments. *Journal of Fluid Mechanics*, *65*, 289–314.

Hérault, A., Bilotta, G., & Dalrymple, R. A. (2010). SPH on GPU with CUDA. *Journal of Hydraulic Research*, *48*(S1), 74–79.

Ichinose, G., Thio, H. K., Sommerfeld, P. G., Sato, T., & Ishii, T. (2003). Rupture process of the 1944 Tonankai earthquake (M$_S$ 8.1) from the inversion of teleseismic and regional seismograms. *Journal of Geophysical Research*, *108*(B10), 2497. https://doi.org/10.1029/2003JB002393

Ichiye, T. (1958). A theory on the generation of tsunamis by an impulse at the sea bottom. *Journal of the Oceanographical Society of Japan*, *14*, 41–44.

Ishii, M., Shearer, P. M., Houston, H., & Vidale, J. E. (2005). Extent, duration and speed of the 2004 Sumatra–Andaman earthquake imaged by the HI-net array. *Nature*, *435*(7044), 933.

Jamin, T., Gordillo, L., Ruiz-Chavarría, G., Berhanu, M., & Falcon, E. (2015). Experiments on generation of surface waves by an underwater moving bottom. *Proceedings of the Royal Society A*, *471*, 20150069.

Kajiura, K. (1963). The leading wave of a tsunami. *Bulletin of the Earthquake Research Institute*, *41*, 535–571.

Kajiura, K. (1972). The directivity of energy radiation of the tsunami generated in the vicinity of a continental shelf. *Journal of Oceanography*, *28*, 260–277.

Kanamori, H. (1972). Determination of effective tectonic stress associated with earthquake faulting. The Tottori earthquake of 1943. *Physics of the Earth and Planetary Interiors*, *5*, 426–434.

Kanamori, H., & Anderson, D. L (1975). Theoretical basis of some empirical relations in seismology. *Bulletin of the Seismological Society of America*, *65*, 1073–1095.

Kervella, Y., Dutykh, D., & Dias, F. (2007). Comparison between three-dimensional linear and nonlinear tsunami generation models. *Theoretical and Computational Fluid Dynamics*, *21*, 245–269.

Monaghan, J. J. (1992). Smoothed particle hydrodynamics. *Annual Review of Astronomy and Astrophysics*, *30*, 543–574.

Monaghan, J. J. (1994). Simulating free surface flows with SPH. *Journal of Computational Physics*, *110*(2), 399–406.

Monaghan, J. J. (2005). Smoothed particle hydrodynamics. *Reports on Progress in Physics*, *68*(8), 1703.

Muhari, A., Imamura, F., Koshimura, S., & Post, J. (2011). Examination of three practical run-up models for assessing tsunami impact on highly populated areas. *Natural Hazards and Earth System Sciences*, *11*, 3107–3123.

Ni, S., Kanamori, H., & Helmberger, D. (2005). Seismology: Energy radiation from the Sumatra earthquake. *Nature*, *434*(7033), 582.

Nosov, M. A. (1999). Tsunami generation in compressible ocean. *Physics and Chemistry of the Earth*, *24*, 437–441.

Nosov, M. A. (2014). Tsunami waves of seismic origin: The modern state of knowledge. *Izvestiya, Atmospheric and Oceanic Physics*, *50*, 474–484.

Nosov, M. A., & Kolesov, S. V. (2007). Elastic oscillations of water column in the 2003 Tokachi-Oki tsunami source: In-situ measurements and 3-D numerical modelling. *Natural Hazards and Earth System Sciences*, *7*, 243–249.

Okal, E. A (1988). Seismic parameters controlling far-field tsunami amplitudes: A review. *Natural Hazards*, *1*, 67–96.

Okal, E. A. (2003). Normal mode energetics for far-field tsunamis generated by dislocations and landslides. *Pure Applied Geophysics*, *160*, 2189–2221.

Okal, E. A., & Synolakis, C. E. (2004). Source discriminants for near-field tsunamis. *Geophysical Journal International*, *158*, 899–912.

Okal, E. A., & Synolakis, C. E. (2008). Far-field tsunami hazard from mega-thrust earthquakes in the Indian Ocean. *Geophysical Journal International*, *172*, 995–1015.

Okal, E. A., & Synolakis, C. E. (2016). Sequencing of tsunami waves: Why the first wave is not always the largest. *Geophysical Journal International*, *204*, 719–735.

Park, H., Cox, D. T, Lynett, P. J., Wiebe, D. M., & Shin, S. (2013). Tsunami inundation modeling in constructed environments: A physical and numerical comparison of free-surface elevation, velocity, and momentum flux. *Coastal Engineering*, *79*, 9–21.

Saito, T., & Furumura, T. (2009). Three-dimensional tsunami generation simulation due to sea-bottom deformation and its interpretation based on linear theory. *Geophysical Journal International*, *178*, 877–888.

Schwartz, S. Y., & Rokosky, J. M. (2007). Slow slip events and seismic tremor at circum-Pacific subduction zones. *Reviews of Geophysics*, *45*, 32. https://doi.org/10.1029/2006RG000208

Shimozono, T., Cui, H., Pietrzak, J. D., Fritz, H. M., Okayasu, A., & Hooper, A. J (2014). Short wave amplification and extreme runup by the 2011 Tohoku tsunami. *Pure and Applied Geophysics*, *171*, 3217–3228.

Son, S., Lynett, P. J., & Kim, D. (2011). Nested and multi-physics modeling of tsunami evolution from generation to inundation. *Ocean Modelling*, *38*, 96–113.

Stefanakis, T. S., Dias, F., & Synolakis, C. (2015). Tsunami generation above a sill. *Pure and Applied Geophysics*, *172*, 985–1002.

Stoker, J. J. (1957). *Water waves: The mathematical theory with applications* (Vol. 36). New York: Interscience.

Synolakis, C. E. (1991). Green's law and the evolution of solitary waves. *Physics of Fluids*, *3*, 490–491.

Synolakis, C. E. (2003). Tsunami and seiche, *Earthquake eng. handbook* (pp. 9_1–9_90). Singapore: CRC Press.

Titov, V., Rabinovich, A. B., Mofjeld, H. O., Thomson, R. E., & González, F. I. (2005). The global reach of the 26 December 2004 Sumatra tsunami. *Science*, *309*, 2045–2048.

Voit, S. (1987). Tsunamis. *Annual Review of Fluid Mechanics*, *19*, 217–236.

Ward, S. N. (1980). Relationships of tsunami generation and an earthquake source. *Journal of Physics of the Earth*, *28*, 441–474.

Ward, S. N. (2001). Landslide tsunami. *Journal of Geophysical Research*, *106*(B6), 11,201–11,215.

Wei, Z., Dalrymple, R. A., Hérault, A., Bilotta, G., Rustico, E., & Yeh, H. (2015). SPH modeling of dynamic impact of tsunami bore on bridge piers. *Coastal Engineering*, *104*, 26–42.

Wei, Z., Dalrymple, R. A., Rustico, E., Hérault, A., & Bilotta, G. (2016). Simulation of nearshore tsunami breaking by smoothed particle hydrodynamics method. *Journal of Waterway, Port, Coastal, and Ocean Engineering*, *142*, 5016001.

Wei, Z., Dalrymple, R. A., Xu, M., Garnier, R., & Derakhti, M. (2017). Short-crested waves in the surf zone. *Journal of Geophysical Research: Oceans*, *122*, 4143–4162. https://doi.org/10.1002/2016JC012485

Willmott, C. J. (1981). On the validation of models. *Physical Geography*, *2*, 184–194.